Couple stress and Darcy Forchheimer hybrid nanofluid flow on a vertical plate by means of double diffusion Cattaneo–Christov analysis

Hamdi Ayed[1,2,†]

[1] *Department of Civil Engineering, College of Engineering, King Khalid University, Abha* 61421, *Kingdom of Saudi Arabia*
[2] *Higher Institute of Transport and Logistics of Sousse, University of Sousse, Sousse* 4023, *Tunisia*

(Received 24 April 2022; revised manuscript received 10 June 2022; accepted manuscript online 27 June 2022)

A three-dimensional Darcy Forchheimer mixed convective flow of a couple stress hybrid nanofluid flow through a vertical plate by means of the double diffusion Cattaneo–Christov model is presented in this study. The influence of high-order velocity slip flow, as well as a passive and active control, is also considered. The motive of the research is to develop a computational model, using cobalt ferrite ($CoFe_2O_4$) and copper (Cu) nanoparticles (NPs) in the carrier fluid water, to magnify the energy and mass communication rate and boost the efficiency and performance of thermal energy conduction for a variety of commercial and biological purposes. The proposed model becomes more significant, with an additional effect of non-Fick's mass flux and Fourier's heat model to report the energy and mass passage rate. The results are obtained through the computational strategy parametric continuation method. The figures are plotted to reveal the physical sketch of the obtained solution, while the statistical assessment has been evaluated through tables. It has been observed that the dispersion of Cu and $CoFe_2O_4$ NPs to the base fluid significantly enhances the velocity and thermal conductivity of water, which is the most remarkable property of these NPs from the industrial point of view.

Keywords: hybrid nanofluid, high order slip, couple stress fluid, non-Fourier's heat and mass flux, Darcy Forchheimer effect

PACS: 02.60.Lj **DOI:** 10.1088/1674-1056/ac7bfb

1. Introduction

Electronic device cooling, heating systems, sustainable energy, constructing shielding, geomorphological systems, non-Newtonian physiochemical processes, electrodynamics, and subsurface therapeutic interventions of atomic or non-nuclear waste are just a few of the applications of hybrid nanofluid (HNF) flow across a permeable vertical plate in chemical, civil, and advanced manufacturing.[1–3] In all of these systems, amplification of heat passage from an energy-saving aspect is of the specific interest. Heat transfer can be enhanced through a variety of techniques, such as changing the flow shape, changing the model parameters, or enhancing the thermal efficiency of the fluid. Suspending higher thermal stability micro powder granules increases base fluid energy conduction qualities, according to several theoretical and practical studies.[4,5] Kumar *et al.*[6] numerically computed the flow of nanofluids and energy conduction over a vertical infinite plate, in the presence of a magnetic field and thermal radiation. It was discovered that increasing the value of the radiation factor improves the velocity and heat flux. Haq *et al.*[7] investigated the energy and mass translocation of an unsteady Newtonian viscous fluid flow across an indefinite vertical surface with variable tensile stress that was modified over time. The numerical simulation of HNF consisting of Al_2O_3–H_2O nanoparticles (NPs) over a vertical flat plate was reported by Mahanthesh *et al.*[8] The addition of Al_2O_3 NPs in water at a 3% of concentration by volume efficiently accelerates the system's heat transfer. Acharya *et al.*[9] depicted the radiative couple stress fluid flowing across a permeable stretched vertical sheet under the upshot of variable viscosity and magnetic conditions. The couple stress variable causes the Nusselt number to decrease by 19.05%, while heat transfer increases by 1.67% for radiation. The generalized Fick's and Fourier's laws have been tested on the MHD couple-stress ferrofluid flows across free convection flow stretchable sheet by Waqas *et al.*[10] Couple-stress nanofluids are beneficial for investigating various sorts of thermal and rheological properties, as these improved fluids can realistically elucidate the dynamical behavior of various liquids, such as polymeric suspensions and human blood. Some more related studies are found in Refs. [11–14].

Several researchers have presented the theoretical and experimental approaches to the above-stated purposes and tasks. Bilal *et al.*[15] reported the properties of magnetic and electric influences on the flow of water-based ferric oxides and CNTs hybrid NFs over double orbiting planes. It was noticed that the velocity boundary layer is boosted by the upshot of the electric variable, while the thermal component is reduced. Ramesh *et al.*[16] used Fe_3O_4 and $CoFe_2O_4$ in EG + water to study the cationic bond formation and enthalpy features in the flow of hybrid NF across a stream-wise region. Ullah *et al.*[17] used

†Corresponding author. E-mail: hayed@kku.edu.sa
© 2023 Chinese Physical Society and IOP Publishing Ltd

a CNT-Fe_3O_4 HNF to simulate the impacts of metallic foam and nanomaterials on the thermal performance of a semisolid heat sink. Using quantitative computations, Ibrahim *et al.*[18] evaluated the influence of distorted circular tubes on improving energy analysis efficacy, as well as the hydrological effectiveness of Cu/water HNF in solar accumulation. Ullah *et al.*[19] studied the effect of concave and convex form on the flow of a radiative hybrid NF (SiO_2-MoS_2/water). When the volume proportion of SiO_2 nanoclusters is increased from 1% to 5%, the thermal efficiency increases by 15.47% for flow over convex-shaped sheets and 14.28% for flow over beveled edge sheets. Wang *et al.*[20] describe how to make noble metal cross-linked materials with nanoscale-dispersed active sites. One of the most Fe/Co-based trifunctional electrode materials yet described has been discovered: the $FeZn_4Co$/CNFs electro catalyst. Gul *et al.*[21,22] used magnetic ferrite and copper nanoparticles to investigate the effect of the hybrid nanofluid in heat transport through a plate-cone viscometer. Ahmadian *et al.*[23,24] investigated a 3D theoretical simulation of an unstable Ag–MgO HNF flow with energy and mass conversion generated by the upward/downward movement of a curvy disc. The insertion of nanocomposites into base fluid has been noticed to increase the carrier fluid's thermal properties dramatically. Ullah *et al.*[25] used Cu and ($CoFe_2O_4$) NPs to analyze the heat conduction as a hybrid nanofluid flow travels linearly across a parabolic concave solar absorber on the exterior of solar aircraft wings. The Cu-EG nanofluid exhibits lower thermal effectiveness than the Cu–$CoFe_2O_4$–Cu/EG nanofluid, ranging between 3.8% and 4.8%. Khashi'ie *et al.*[26] investigated the MHD HNF flow with energy transmission over a movable plate with thermal radiation, using Cu and metal oxide nano particulate as well as water as the conventional fluids. References [27–30] provide some relevant literature as well as applications of Cu and $CoFe_2O_4$ NPs in water for biological and engineering purposes.

To discuss the behaviors of energy and mass diffusion rates, the Cattaneo–Christov double diffusion (CCDD) idea is adopted. This model is based on the Fourier's and Fick's laws. Hayat *et al.*[31] studied the Prandtl liquid flow in three dimensions in the presence of enhanced heat propagation and mass diffusion concepts. The thermal properties are reducing factors of the concentration and thermal relaxation constants, according to their findings. Li *et al.*[32] used Cattaneo–Christov (CC), thermal flux models, to investigate the impact of MHD hydrodynamic fluid over an extended Riga sheet. It was discovered that the velocity gradient improves with the variation of the ratio component and Hartman number. Ullah *et al.*[33] investigated the Cattaneo–Christov double-diffusion model applied to non-uniformly radiative Walter-B nano liquid flow across an extended sheet with Joule heating processes. The energy conduction rate was noticed to be higher when the thermal relaxation coefficient is increased. Waqas *et al.*[34] used the Fourier's and Fick's laws to analyze the Newtonian nanoliquid flow along an inclined flexible tube under the impacts of the magnetization, kinetic energy, and motile microbes. Some recent related studies to the Cattaneo–Christov double diffusion model and hybrid nanofluid flow can be found in Refs. [35–38].

The aim of the study is to model the 3D Darcy Forchheimer mixed convective flow of a couple stress hybrid nanofluid flow through a vertical plate by means of double diffusion Cattaneo–Christov mode. The purpose is to construct a computational model for the hybrid nanofluid flow consisting of $CoFe_2O_4$ and Cu nanoparticles in the carrier fluid water to boost the efficiency and productivity of thermal energy propagation for a variety of commercial and biological applications.

The novelty of the problem is pointed out as follows.

i) $CoFe_2O_4$ and Cu NPs based hybrid nanofluids are used to improve the heat transfer analysis.

ii) The couple stress is an additional extension to investigate the fluid flow analysis in terms of this parameter.

iii) Non-Fourier heat, and non-Fick's mass flux are used in 3D space and the impact of the relaxation parameters is examined.

iv) Darcy–Forchheimer porous space is considered for the flow pattern.

v) PCM method is used to find the solution of the nonlinear problem.

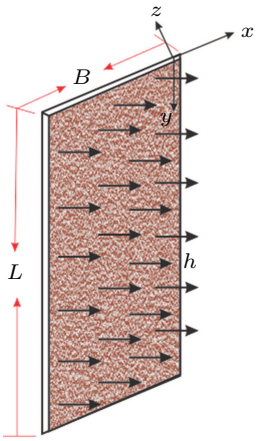


Fig. 1. Flow configuration and coordinate system.

2. Mathematical formulation

In this study, the steady, laminar, and incompressible 3D flow of mixed convection couple stress nanofluid with non-Fourier heat, and non-Fick's mass flux model is considered. The fluid flow is considered Darcy–Forchheimer's porous space.

To model the problem mathematically, x- and y-axes are taken in the direction of motion and the z-axis is normal to

the fluid flow with the direction of magnetic field strength B_0. The velocity $u = ax = U_w(x)$ is the stretching velocity with $a > 0$ and the flow is in the domain of $z > 0$. Also, the ambient temperature T_∞ and ambient concentration C_∞ are assumed to be constant. The velocity components in the (x, y, z) coordinate are assumed as (u, v, w). The effects of non-Fourier's heat flux and non-Fick's mass flux theory, entropy generation, slip flow condition, passive and active control conditions are implemented to the problem to examine the features of flow, heat, and mass transfer. Based on above mentioned assumptions the high order partial differential equations obtained from the governing problem are[39]

$$\frac{\partial u}{\partial x}+\frac{\partial v}{\partial y}+\frac{\partial w}{\partial z}=0, \tag{1}$$

$$\begin{aligned} &u\frac{\partial u}{\partial x}+v\frac{\partial u}{\partial y}+w\frac{\partial u}{\partial z}\\ &=\frac{\mu_{hnf}}{\rho_{hnf}}\frac{\partial^2 u}{\partial z^2}-\frac{\eta^*}{\rho_{hnf}}\frac{\partial^4 u}{\partial z^4}-\frac{\mu_{hnf}}{\rho_{hnf}k^*}u-\frac{C_b}{\sqrt{k^*}}u^2\\ &+g\left[\left(\beta_{Thnf}(T-T_\infty)+\beta_c(C-C_\infty)\right)\right], \end{aligned} \tag{2}$$

$$\begin{aligned} &u\frac{\partial v}{\partial x}+v\frac{\partial v}{\partial y}+w\frac{\partial v}{\partial z}\\ &=\frac{\mu_{hnf}}{\rho_{hnf}}\frac{\partial^2 v}{\partial z^2}-\frac{\eta^*}{\rho_{hnf}}\frac{\partial^4 v}{\partial z^4}-\frac{\mu_{hnf}}{\rho_{hnf}k^*}v-\frac{C_b}{\sqrt{k^*}}v^2, \end{aligned} \tag{3}$$

$$\begin{aligned} &u\frac{\partial T}{\partial x}+v\frac{\partial T}{\partial y}+w\frac{\partial T}{\partial z}+\Lambda_E'\Psi_E\\ &=\frac{k}{(\rho C_p)_{hnf}}\frac{\partial^2 T}{\partial z^2}+\frac{(\rho C_p)_{nf}}{(\rho C_p)_f}\\ &\times\left[D_B\frac{\partial C}{\partial z}\frac{\partial T}{\partial z}+\left(\frac{D_T}{T_\infty}\right)\left(\frac{\partial T}{\partial z}\right)^2\right], \end{aligned} \tag{4}$$

$$\begin{aligned} &u\frac{\partial C}{\partial x}+v\frac{\partial C}{\partial y}+w\frac{\partial C}{\partial z}+\Lambda_C'\Psi_C\\ &=D_B\frac{\partial^2 C}{\partial z^2}+\left(\frac{D_T}{T_\infty}\right)\frac{\partial^2 T}{\partial z^2}. \end{aligned} \tag{5}$$

The subjected boundary conditions are stated as

$$\begin{aligned} &u=U_w(x),\ \ v=0,\ \ w=0,\ \ T=T_w,\ \ C=C_w,\ \text{ at }\ z=0,\\ &u\to 0,\ \ v\to 0,\ \ w\to 0,\ \ T\to T_\infty,\ \ C\to C_\infty,\ \text{ at }\ z\to\infty. \end{aligned} \tag{6}$$

Here β_T is the heat flux expansion coefficient, β_C is the mass flux expansion coefficient, g is the gravitational acceleration, h_f is the heat transfer constant, T_f is the temperature and σ is the electrical conductivity of fluid . Ψ_E and Ψ_C in Eqs. (4) and (5) are defined, respectively, as follows:

$$\begin{aligned} \Psi_E &= u^2\frac{\partial^2 T}{\partial x^2}+v^2\frac{\partial^2 T}{\partial y^2}+w^2\frac{\partial^2 T}{\partial z^2}+2uv\frac{\partial^2 T}{\partial x\partial y}\\ &+2uw\frac{\partial^2 T}{\partial x\partial z}+2vw\frac{\partial^2 T}{\partial y\partial z}\\ &+\left(u\frac{\partial u}{\partial x}+v\frac{\partial u}{\partial y}+w\frac{\partial u}{\partial z}\right)\frac{\partial T}{\partial x}\\ &+\left(u\frac{\partial v}{\partial x}+v\frac{\partial v}{\partial y}+w\frac{\partial v}{\partial z}\right)\frac{\partial T}{\partial y}\\ &+\left(u\frac{\partial w}{\partial x}+v\frac{\partial w}{\partial y}+w\frac{\partial w}{\partial z}\right)\frac{\partial T}{\partial z}, \end{aligned} \tag{7}$$

$$\begin{aligned} \Psi_C &= u^2\frac{\partial^2 C}{\partial x^2}+v^2\frac{\partial^2 C}{\partial y^2}+w^2\frac{\partial^2 C}{\partial z^2}+2uv\frac{\partial^2 C}{\partial x\partial y}\\ &+2uw\frac{\partial^2 C}{\partial x\partial z}+2vw\frac{\partial^2 C}{\partial y\partial z}\\ &+\left(u\frac{\partial u}{\partial x}+v\frac{\partial u}{\partial y}+w\frac{\partial u}{\partial z}\right)\frac{\partial C}{\partial x}\\ &+\left(u\frac{\partial v}{\partial x}+v\frac{\partial v}{\partial y}+w\frac{\partial v}{\partial z}\right)\frac{\partial C}{\partial y}\\ &+\left(u\frac{\partial w}{\partial x}+v\frac{\partial w}{\partial y}+w\frac{\partial w}{\partial z}\right)\frac{\partial C}{\partial z}. \end{aligned} \tag{8}$$

Table 1. The statistical properties of copper, cobalt iron oxide and water.[40,41]

	ρ (kg/m^3)	C_p (J/kg·K)	k (W/mK)
Water	997.1	4179	0.613
Copper Cu	8933	385	401
$CoFe_2O_4$	4907	700	3.7

Employing the resemblance conversion

$$\begin{aligned} &u=axf'(\eta),\quad v=ayg'(\eta),\quad w=-\sqrt{av}(f(\eta)+g(\eta)),\\ &\eta=\sqrt{\frac{a}{v}}z,\quad \theta(\eta)=\frac{T-T_\infty}{T_f-T_\infty},\\ &\Phi(\eta)=\frac{C-C_\infty}{C_w-C_\infty}, \end{aligned} \tag{9}$$

we get

$$\begin{aligned} &f'''+\frac{\rho_{hnf}}{\rho_f}\frac{\mu_f}{\mu_{hnf}}\left[(f+g)f''-(f')^2-Fr(f')^2\right]\\ &-krf'-\frac{\mu_f}{\mu_{hnf}}Kf^{(5)}+\frac{(\rho\beta)_{hnf}}{(\rho\beta)_f}\lambda(\theta+N\Phi)=0, \end{aligned} \tag{10}$$

$$\begin{aligned} &g'''+\frac{\rho_{hnf}}{\rho_f}\frac{\mu_f}{\mu_{hnf}}\left[(f+g)g''-Fr(g')^2\right]\\ &-krg'-\frac{\mu_f}{\mu_{hnf}}Kg^{(5)}=0, \end{aligned} \tag{11}$$

$$\begin{aligned} &\frac{k_{hnf}}{k_f}\theta''+\frac{(\rho cp)_{hnf}}{(\rho cp)_f}Pr\left[(f+g)\theta'+Nb\theta'\Phi'\right.\\ &\left.+Nt(\theta')^2-\delta_t(\theta''+\theta')(f+g)^2\right]=0, \end{aligned} \tag{12}$$

$$\begin{aligned} &\Phi''+\frac{Nt}{Nb}\theta''+Sc(f+g)\Phi'\\ &-\delta_c Sc\left[(f+g)^2\Phi''+(f+g)(f'+g')\Phi'\right]=0, \end{aligned} \tag{13}$$

and the transform conditions

$$\left.\begin{aligned} &f'(0)=1,\quad f(0)=0,\quad g(0)=0,\\ &\theta(0)=\Phi(0)=1,\qquad\qquad\qquad \text{at }\ z=0,\\ &f'(\infty)=f(\infty)=g(\infty)=\theta(\infty)=\Phi(\infty)\to 0,\ \text{at }\ z\to\infty. \end{aligned}\right\} \tag{14}$$

Here Pr is the Prandtl number, N is the mixed convection flow constraint, Nb is the Brownian motion, Sc is the Schmidt number, Nt is the thermophoresis constraint, δ_t is the time relaxation time constant for temperature, δ_c is the time relaxation

constant for particle concentration, K is the couple stress, Fr is the Darcy Forchheimer term, kr is the porosity parameter, λ is the buoyancy parameter, Gr is the Grashof number and Re_x, Re_y are the Reynolds numbers defined as

$$\begin{aligned}
&Pr=\frac{(\rho c)_{\mathrm{f}}\upsilon}{k},\quad N=\frac{\beta_{\mathrm{C}}(C_{\mathrm{w}}-C_{\infty})}{\beta_{\mathrm{T}}(T_{\mathrm{f}}-T_{\infty})},\\
&Nb=\frac{(\rho c)_{nf}(C_{\mathrm{w}}-C_{\infty})}{(\rho c)_{\mathrm{f}}\upsilon},\\
&Sc=P_rLe,\quad Nt=\frac{(\rho c)_{nf}D_{\mathrm{T}}(T_{\mathrm{f}}-T_{\infty})}{(\rho c)_{\mathrm{f}}T_{\infty}},\\
&\delta_{\mathrm{t}}=\Lambda'_{\mathrm{E}}\left(\frac{k}{(\rho c)_{\mathrm{f}}}\right),\quad \delta_{\mathrm{c}}=\Lambda'_{\mathrm{C}}\left(\frac{k}{(\rho c)_{\mathrm{f}}}\right),\\
&K=\frac{\mu^*}{\rho_{\mathrm{f}}}\frac{a}{\upsilon},\quad Fr=\frac{C_{\mathrm{b}}}{\sqrt{k^*}}x,\quad \lambda=\frac{G}{Re_x},\\
&Gr=\frac{gB_{\mathrm{T}}(T_{\mathrm{f}}-T_{\infty})x^3}{\upsilon^2},\quad Re_x^2=\frac{aU_x}{\upsilon},\quad Re_y^2=\frac{aU_y}{\upsilon}.
\end{aligned}\tag{15}$$

The skin-friction $(C_{\mathrm{fx}},C_{\mathrm{fy}})$, local Nusselt number (Nu_x) and the local Sherwood number (Sh_x) are defined as

$$\begin{aligned}
&C_{\mathrm{fx}}=\frac{\tau_{\mathrm{w}x}}{\rho U_{\mathrm{w}x}^2},\quad C_{\mathrm{fy}}=\frac{\tau_{\mathrm{wy}}}{\rho V_{\mathrm{wy}}^2},\\
&Nu_x=\frac{xq_{\mathrm{w}}}{k_{\mathrm{f}}(T_{\mathrm{f}}-T_{\infty})},\quad Sh_x=\frac{xh_m}{k(C_{\mathrm{w}}-C_{\infty})},
\end{aligned}\tag{16}$$

where the wall shear stress

$$\tau_{\mathrm{w}x}=\left(\mu\frac{\partial u}{\partial z}-\mu^*\frac{\partial^3 u}{\partial z^3}\right)_{z=0},\quad \tau_{\mathrm{wy}}=\left(\mu\frac{\partial u}{\partial z}-\mu^*\frac{\partial^3 u}{\partial z^3}\right)_{z=0},$$

heat flux $q_{\mathrm{w}}=-k(\partial T/\partial z)_{z=0}$ and wall mass flux $h_{\mathrm{w}}=-D_{\mathrm{B}}(\partial C/\partial z)_{z=0}$ in the dimensionless form are expressed as

$$\begin{aligned}
&\sqrt{Re_x}C_{\mathrm{fx}}=f''(0)-Kf''''(0)=0,\\
&\sqrt{Re_y}C_{\mathrm{fy}}=g''(0)-Kg''''(0)=0,\\
&\frac{Nu_x}{\sqrt{Re_x}}=-\theta'(0),\quad \frac{Sh_x}{\sqrt{Re_x}}=-\phi'(0).
\end{aligned}\tag{17}$$

3. Numerical solution

The researchers used several numerical and computational methods[42–50,53] to find the solution to different models. Our work also depends on the computational analysis PCM. The basic strategy of applying PCM are presented as follows.[54–59]

Step 1: Reducing the BVP to a first-order system of ODEs

For this purpose, we introduce the following functions:

$$\left.\begin{aligned}
&\hbar_1=f(\eta),\quad \hbar_2=f'(\eta),\quad \hbar_3=f''(\eta),\quad \hbar_4=g(\eta),\quad \hbar_5=g'(\eta),\\
&\hbar_6(\eta)=g''(\eta),\quad \hbar_7=\theta(\eta),\quad \hbar_8=\theta'(\eta),\quad \hbar_9=\Phi(\eta),\quad \hbar_{10}=\Phi'(\eta).
\end{aligned}\right\}\tag{18}$$

Putting Eqs. (18) in Eqs. (10)–(13) and (14), we get

$$\hbar'_3+\frac{\rho_{hnf}}{\rho_{\mathrm{f}}}\frac{\mu_{\mathrm{f}}}{\mu_{hnf}}\left[(\hbar_1+\hbar_4)\,\hbar_3-(\hbar_2)^2-Fr(\hbar_2)^2\right]-kr\,\hbar_2-\frac{\mu_{\mathrm{f}}}{\mu_{hnf}}K\,\hbar_1^{(5)}+\frac{(\rho\beta)_{hnf}}{(\rho\beta)_{\mathrm{f}}}\lambda(\hbar_7+N\,\hbar_9)=0,\tag{19}$$

$$\hbar'_6+\frac{\rho_{hnf}}{\rho_{\mathrm{f}}}\frac{\mu_{\mathrm{f}}}{\mu_{hnf}}\left[(\hbar_1+\hbar_4)\,\hbar_6-Fr(\hbar_5)^2\right]-kr\,\hbar_5-\frac{\mu_{\mathrm{f}}}{\mu_{hnf}}K\,\hbar_4^{(5)}=0,\tag{20}$$

$$\left(\frac{k_{hnf}}{k_{\mathrm{f}}}+\frac{\delta_{\mathrm{t}}(\rho cp)_{hnf}}{(\rho cp)_{\mathrm{f}}}Pr\right)\hbar'_8+\frac{(\rho cp)_{hnf}}{(\rho cp)_{\mathrm{f}}}Pr\left[(\hbar_1+\hbar_4)+Nb\,\hbar_{10}+Nt(\hbar_8)-\delta_{\mathrm{t}}(\hbar_1+\hbar_4)^2\right]\hbar_8=0,\tag{21}$$

$$\left(1-Sc(\hbar_1+\hbar_4)^2\right)\hbar'_{10}+Sc(\hbar_1+\hbar_4)[1-\delta_{\mathrm{c}}(\hbar_2+\hbar_5)]\,\hbar_{10}+\frac{Nt}{Nb}\hbar'_8-\delta_{\mathrm{c}}Sc(\hbar_1+\hbar_4)^2=0,\tag{22}$$

and the transform conditions

$$\left.\begin{aligned}
&\hbar_2(0)=1,\quad \hbar_1(0)=0,\quad \hbar_4(0)=0,\quad \hbar_7(0)=\hbar_9(0)=1,\\
&\hbar_2(\infty)=\hbar_1(\infty)=\hbar_4(\infty)=\hbar_7(\infty)=\hbar_9(\infty)\to 0.
\end{aligned}\right\}\tag{23}$$

Step 2: Introducing parameter p

$$\hbar'_3+\frac{\rho_{hnf}}{\rho_{\mathrm{f}}}\frac{\mu_{\mathrm{f}}}{\mu_{hnf}}\left[\frac{(\hbar_1+\hbar_4)(\hbar_3-1)}{p}-(\hbar_2)^2-Fr(\hbar_2)^2\right]-kr\,\hbar_2-\frac{\mu_{\mathrm{f}}}{\mu_{hnf}}K\,\hbar_1^{(5)}+\frac{(\rho\beta)_{hnf}}{(\rho\beta)_{\mathrm{f}}}\lambda(\hbar_7+N\,\hbar_9)=0,\tag{24}$$

$$\hbar'_6+\frac{\rho_{hnf}}{\rho_{\mathrm{f}}}\frac{\mu_{\mathrm{f}}}{\mu_{hnf}}\left[(\hbar_1+\hbar_4)(\hbar_6-1)p-Fr(\hbar_5)^2\right]-kr\,\hbar_5-\frac{\mu_{\mathrm{f}}}{\mu_{hnf}}K\,\hbar_4^{(5)}=0,\tag{25}$$

$$\left(\frac{k_{hnf}}{k_{\mathrm{f}}}+\frac{\delta_{\mathrm{t}}(\rho cp)_{hnf}}{(\rho cp)_{\mathrm{f}}}Pr\right)\hbar'_8+\frac{(\rho cp)_{hnf}}{(\rho cp)_{\mathrm{f}}}Pr\left[(\hbar_1+\hbar_4)+Nb\,\hbar_{10}+Nt(\hbar_8)-\delta_{\mathrm{t}}(\hbar_1+\hbar_4)^2\right](\hbar_8-1)p=0,\tag{26}$$

$$\left(1-Sc(\hbar_1+\hbar_4)^2\right)\hbar'_{10}+Sc(\hbar_1+\hbar_4)[1-\delta_{\mathrm{c}}(\hbar_2+\hbar_5)](\hbar_{10}-1)p+\frac{Nt}{Nb}\hbar'_8-\delta_{\mathrm{c}}Sc(\hbar_1+\hbar_4)^2=0.\tag{27}$$

Step 3: Differentiating by parameter *p*

After differentiating Eqs. (24)–(27) with respect to parameter p, it arrives at the following system with respect to sensitivities to the parameter p

$$V' = AV + R, \tag{28}$$

where A is the coefficient matrix, R is the remainder and

$$V = \frac{\mathrm{d}\zeta_i}{\mathrm{d}\tau}, \tag{29}$$

where $i = 1, 2, \ldots, 11$.

Step 4: Apply superposition principle and specify Cauchy problem for each component

$$V = aU + W, \tag{30}$$

where U and W are unknown vector functions with

$$U = aU, \tag{31}$$

$$W' = AW + R. \tag{32}$$

Putting the approximate solution Eq. (32) into the original Eq. (30), we obtain

$$(aU + W)' = A(aU + W) + R. \tag{33}$$

Step 5: Solving the Cauchy problems

Numerical implicit scheme is used in this work, which is presented as below.

From Eqs. (31) and (32) we have

$$\frac{U^{i+1} - U^i}{\Delta\eta} = AU^{i+1}, \quad \text{or} \quad (I - \Delta\eta A)U^{i+1} = U^i, \tag{34}$$

$$\frac{W^{i+1} - W^i}{\Delta\eta} = AW^{i+1}, \quad \text{or} \quad (I - \Delta\eta A)W^{i+1} = W^i, \tag{35}$$

from which the iterative form of the solution are obtained as

$$U^{i+1} = (I - \Delta\eta A)^{-1}U^i, \tag{36}$$

$$W^{i+1} = (I - \Delta\eta A)^{-1}(W^i + \Delta\eta R). \tag{37}$$

4. Results and discussion

The discussion section analyzes the behavior of velocity, temperature and concentration distribution alongside the variation of several physical constraints for HNF comprised of Cu and $CoFe_2O_4$ nanoparticles. Their out-turns are revealed through the comparative Figs. 2–15 and Tables.

Figures 2–6 revealed the presentation of axial velocity profile $(f'(\eta))$ versus the variation of buoyancy force parameter λ, mixed connection term N, Darcy Forchheimer term Fr, couple stress parameter K and volume friction constraints (ϕ_1, ϕ_2), respectively. Figures 2 and 3 highlighted that the velocity profile enhances with the effect of buoyancy force parameter λ and the mixed connection term N. Because of the composition of the mixed convection component, it can be deduced that it is the ratio of inertia force to buoyancy force. When buoyancy force dominates inertia force, the mixed convection factor increases. As a result of the increase in N, the fluid flow in the region is accelerated as shown in Fig. 3. Figures 4 and 5 display that the velocity field diminishes with the increment of Darcy Forchheimer term Fr and boosts with the influence of couple stress parameter K. The couple stress component is determined by the couple stress viscosity and functions as a retarding factor, making the fluid denser and causing an increase in fluid velocity. It follows from Fig. 2 that increasing the couple stress constraint K leads the fluid in the flow zone to move faster. Figure 6 revealed that the velocity profile significantly elevated with the inclusion of copper ϕ_1 and cobalt ferrite ϕ_2 nanoparticles in the water. The specific heat capacity of water is greater than Cu and $CoFe_2O_4$ NPs. That is why its inclusion encourages the fluid velocity as shown in Fig. 6.

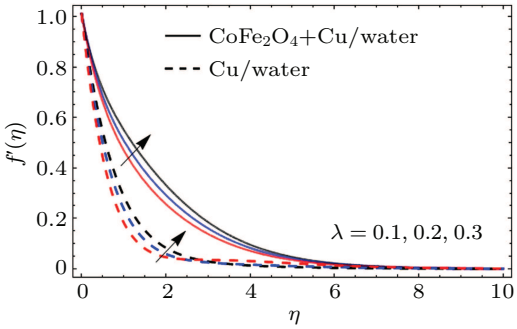


Fig. 2. Presentation of velocity profile $f'(\eta)$ versus buoyancy force parameter λ.

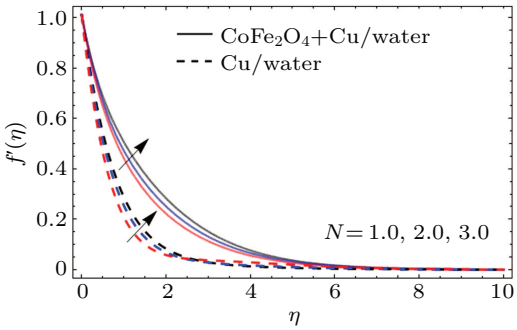


Fig. 3. Presentation of velocity profile $f'(\eta)$ versus mixed connection term N.

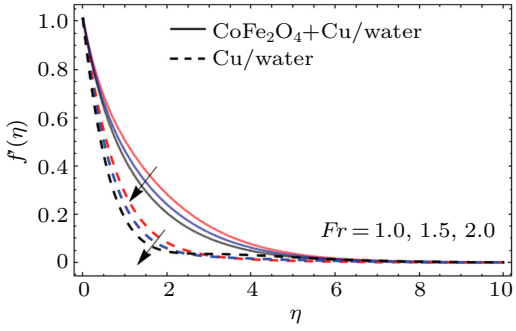


Fig. 4. Presentation of velocity profile $f'(\eta)$ versus Darcy Forchheimer term Fr.

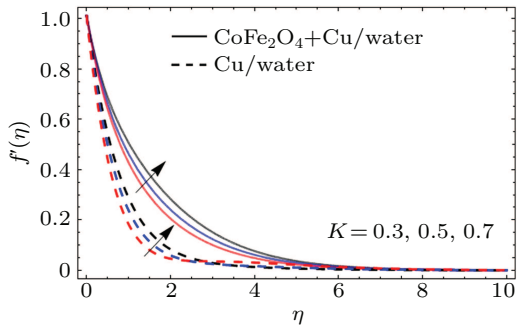


Fig. 5. Presentation of velocity profile $f'(\eta)$ versus couple stress parameter K.

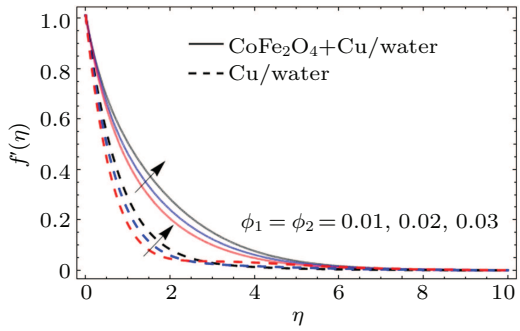


Fig. 6. Presentation of velocity profile $f'(\eta)$ versus volume friction constraints (ϕ_1, ϕ_2).

Figures 7 and 8 revealed the demonstration of radial velocity profile $(g'(\eta))$ versus the variation of Darcy Forchheimer term *Fr* and couple stress parameter *K*. Figures 7 and 8 presented that the fluid velocity in radial direction also declines with the Darcy Forchheimer effect, while augmented with the flourishing values of couple stress parameter. The similar trend has been observed for radial velocity against the couple stress as in Fig. 5.

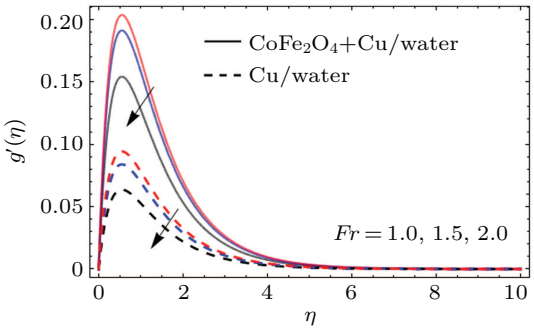


Fig. 7. Presentation of velocity profile $g'(\eta)$ versus Darcy Forchheimer term *Fr*.

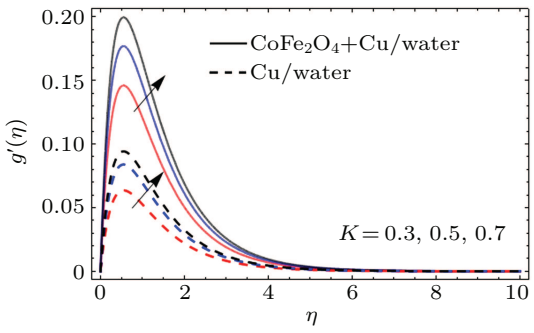


Fig. 8. Presentation of velocity profile $g'(\eta)$ versus couple stress term *K*.

Figures 9–13 elaborated the presentation of energy profile $\theta(\eta)$ versus volume friction constraints (ϕ_1, ϕ_2), thermophoresis *Nt*, Brownian motion *Nb*, mixed convection term *N* and versus time relaxation constraint for energy δ_t respectively. Figure 9 reported that the energy profile magnifies with the rising quantity of NPs in the carrier fluid. Physically, the thermal conductivity of water (0.613 W/m·K) is much smaller than $CoFe_2O_4$ (3.7 W/m·K) and Cu (401 W/m·K) NPs. That is why the inclusion of these particles in the base fluid, elevated its average thermal conductivity, which is the most tremendous property of proposed nanoparticles for industrial and biomedical applications.

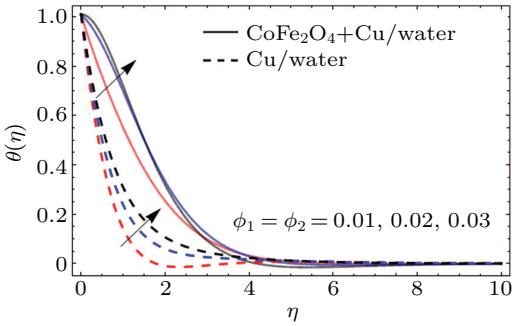


Fig. 9. Presentation of energy profile $\theta(\eta)$ versus volume friction constraints (ϕ_1, ϕ_2).

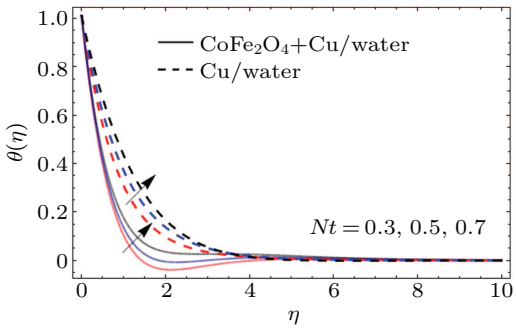


Fig. 10. Presentation of energy profile $\theta(\eta)$ versus thermophoresis constraint *Nt*.

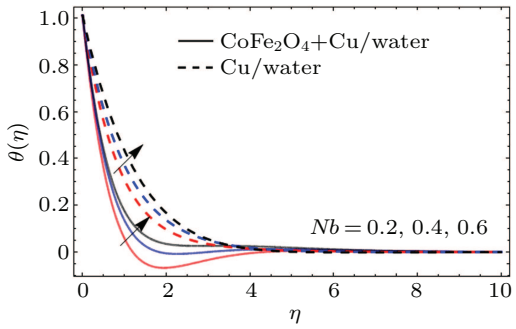


Fig. 11. Presentation of energy profile $\theta(\eta)$ versus Brownian motion constraint *Nb*.

Figures 10 and 11 manifested that the thermal energy profile augmented with the rising credit of thermophoresis *Nt* and Brownian motion *Nb*. It has been discovered that when Brownian motion increases, the random motion of nanocrystals intensifies, resulting in the expansion of the thermal boundary

layer of HNF flow. The kinetic energy of hybrid nanofluid particles is converted to thermal energy throughout the flow motion. As a result, an increase in *Nt* and *Nb* causes a rise in temperature as seen in Figs. 10 and 11. Figures 12 and 13 illustrated that the effect of both mixed convection term *N* and time relaxation constraint for energy δ_t diminish the temperature distribution $\theta(\eta)$. In terms of physics, an increase in the mixed convection variable in the flow region causes the buoyancy force to rule the inertia force, which boosts the heat transfer rate. As a result, the temperature variation and the thickness of the boundary layer appear to be decreasing.

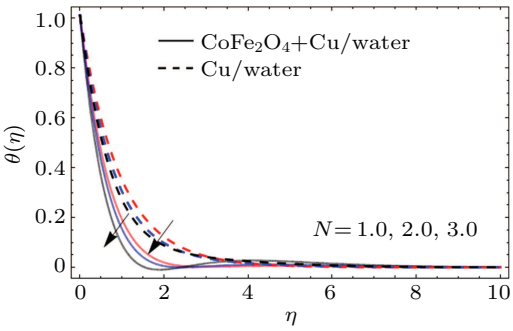


Fig. 12. Presentation of energy profile $\theta(\eta)$ versus mixed convection constraint *N*.

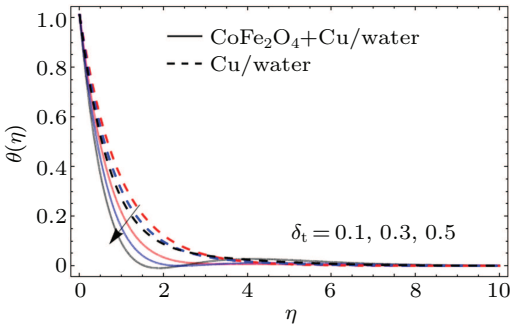


Fig. 13. Presentation of energy profile $\theta(\eta)$ versus time relaxation constraint for energy δ_t.

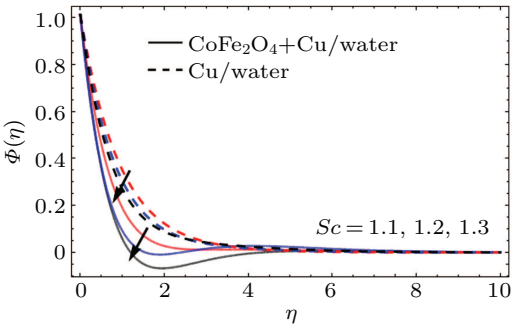


Fig. 14. Presentation of concentration profile $\Phi(\eta)$ versus Schmidt number *Sc*.

Figures 14 and 15 illustrated the concentration profile $\Phi(\eta)$versus Schmidt number *Sc* and time relaxation constraint for mass δ_c. The kinetic viscosity of fluid enhances with the flourishing values of Schmidt number, while reduces the molecular diffusion, and that is why the mass profile declines with the effect of Schmidt number. The concentration also declines with the upshot of δ_t. This is because a decrease in the δ_t causes an increase in mass flux retardation time and, as a result, a decrease in concentration occurred. Tables 2 and 3 displays the statistical outputs of skin friction $(-f''(0), -g''(0))$, Nusselt number $Re^{-1/2}Nu_x$ and Sherwood $Re^{-1/2}Sh_x$ versus different physical parameters.

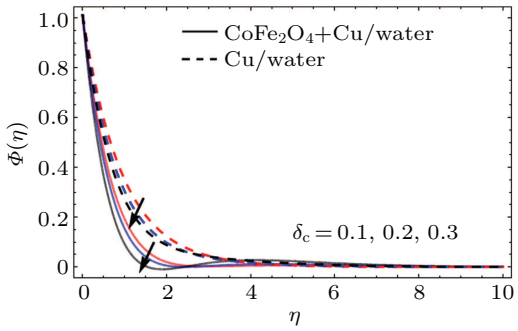


Fig. 15. Presentation of concentration profile $\Phi(\eta)$ versus time relaxation constraint for mass δ_c.

The heat transfer rate increases with the augmentation of the nanoparticle volume fraction as shown in Fig. 16. The result shows that the increasing amount of the nanoparticle volume fraction is more effective by using hybrid nanofluids instead of nanofluids. The percentage enhancement in the heat transfer with the rising values of the nanoparticle volume fraction is shown in Fig. 17. The obtained results show that hybrid nanofluids increase the heat transfer rate more effectively as compared to traditional fluids.

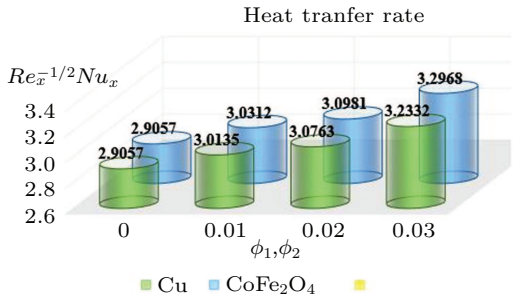


Fig. 16. Nanoparticle volume fraction versus heat transfer rate.

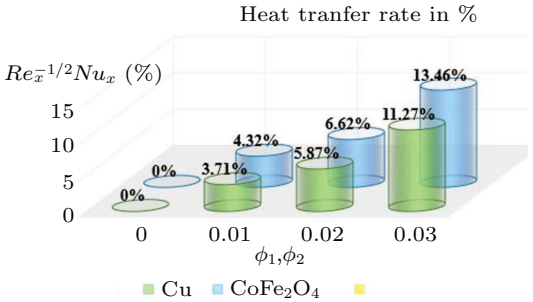


Fig. 17. Nanoparticle volume fraction versus heat transfer rate enhancement in %.

Table 2. Statistical assessment of local skin-friction $(-f''(0), -g''(0))$ constant versus several physical parameters.

K	Fr	N	λ	$-f''(0)$	$-g''(0)$
1.0	0.1	0.01	0.1	0.873605	0.615032
1.1				0.863006	0.605402
1.3				0.857117	0.599296
1.5				0.853587	0.595110
1.0	0.6			0.856407	0.708780
	0.7			0.838751	0.799101
	0.8			0.820613	0.885820
	0.5	0.02		0.874187	0.615036
		0.03		0.874768	0.615044
		0.04		0.875348	0.615052
			0.2	1.004975	0.615348
			0.3	1.046528	0.615673
			0.4	1.088269	0.616004
			0.1	0.871326	0.627791

Table 3. Numerical assessment of $Re^{-1/2}Nu_x$ & $Re^{-1/2}Sh_x$ versus physical quantities.

δ_t	δ_c	N	Nb	Nt	λ	$Re^{-1/2}Nu_x$	$Re^{-1/2}Sh_x$
0.1	0.2	0.1	0.2	0.1	0.1	0.632292	0.659931
0.2						0.625678	0.677716
0.3						0.619718	0.697878
0.4						0.613998	0.721236
	0.3					0.632164	0.653266
	0.4					0.632001	0.646833
	0.5					0.631801	0.640778
	0.2	0.2				0.613991	0.632287
		0.3				0.632283	0.659934
		0.4				0.632278	0.659936
		0.1	0.4			0.632293	0.714866
			0.6			0.632294	0.753148
			0.8			0.632294	0.781039
			0.2	0.2		0.631398	0.654388
				0.3		0.630506	0.650974
				0.4		0.629606	0.649652
				0.1	0.3	0.632352	0.659952
					0.5	0.632406	0.659979
					0.7	0.632468	0.660011
					0.1	0.703042	0.659931

5. Conclusion

The intention of present work is to examine a 3D Darcy Forchheimer mixed convective flow of a couple stress hybrid nanofluid flow through a vertical sheet. The hybrid nanofluid has been synthesized with the inclusion of cobalt ferrite $CoFe_2O_4$ and Cu NPs in the water. The model becomes more meaningful, with the addition of Fick's flux and Fourier's heat model to describe the energy and mass passage rate. The phenomena have been stated in the form of a highly nonlinear system of PDEs, which are then renovated to a dimensionless system of ODEs by using a suitable similarity substitution. The results are produced by using the parametric continuation method of computational strategy. The following observation have been noticed.

The axial velocity profile $(f'(\eta))$ enhances with the effect of buoyancy force parameter, mixed connection term, and couple stress, while reducing with the effect of Darcy Forchheimer term.

The dispersion of Cu and $CoFe_2O_4$ NPs to the base fluid significantly enhances the velocity and thermal conductivity of water, which is the most remarkable property of these NPs from the industrial point of view.

The radial velocity profile $(g'(\eta))$ declines with the Darcy Forchheimer effect, while augmented with the flourishing values of couple stress parameter.

The energy profile $\theta(\eta)$ magnifies with the rising values of thermophoresis Nt and Brownian motion parameter, while diminishing with the upshot of convection term and time relaxation constraint for energy.

The concentration profile $\Phi(\eta)$ reduces with the influence of both Schmidt number Sc and time relaxation constraint for mass δ_c.

The obtained results show that hybrid nanofluids are more effective to enhance heat transfer as compared to traditional fluids. The % wise improvement in the heat transfer rate also validate the obtained results.

Data availability statement

The data that support the findings of this study are available from the corresponding author upon reasonable request.

Acknowledgement

The authors extend their appreciation to the Deanship of Scientific Research at King Khalid University for funding this work through Large Groups Project under grant number (RGP.2/155/43).

References

[1] Algehyne E A, Areshi M, Saeed A, Bilal M, Kumam W and Kumam P 2022 *Scientific Reports* **12** 1
[2] Shuaib M, Bilal M and Qaisar S 2020 *Physica Scripta* **96** 025201
[3] Xu Y J, Bilal M, Al-Mdallal Q, Khan M A and Muhammad T 2021 *Scientific Reports* **11** 1
[4] Tassaddiq A, Khan S, Bilal M, Gul T, Mukhtar S, Shah Z and Bonyah E 2020 *AIP Advances* **10** 055317
[5] Gul T, Rahman J U, Bilal M, Saeed A, Alghamdi W, Mukhtar S and Bonyah E 2020 *AIP Advances* **10** 105308
[6] Kumar M A, Reddy Y D, Rao V S and Goud B S 2021 *Case studies in thermal engineering* **24** 100826
[7] Haq S U, Shah S I A, Nisar K S, Jan S U and Khan I 2021 *Scientific Reports* **11** 1
[8] Mahanthesh B, Mackolil J, Radhika M, Al-Kouz W and Siddabasappa 2021 *Int. Commun. Heat Mass Transfer* **120** 105029
[9] Acharya N, Mondal H and Kundu P K 2021 *Proceedings of the Institution of Mechanical Engineers, Part C: Journal of Mechanical Engineering Science* **235** 2692
[10] Waqas H, Wakif A, Al-Mdallal Q, Zaydan M, Farooq U and Hussain M 2022 *Alexandria Engineering Journal* **61** 1425
[11] Elattar S, Helmi M M, Elkotb M A, El-Shorbagy M A, Abdelrahman A, Bilal M and Ali A 2022 *Alexandria Engineering Journal* **61** 10319
[12] Nazeer M, Hussain F, Khan M I, El-Zahar E R, Chu Y M and Malik M Y 2022 *Applied Mathematics and Computation* **420** 126868
[13] Zhao T H, Wang M K, Hai G J And Chu Y M 2022 *Revista de la Real Academia de Ciencias Exactas, Físicas y Naturales. Serie A. Matemáticas* **116** 1

[14] Zhao T H, Ijaz Khan M and Chu Y M 2023 *Math. Methods Appl. Sci.* **46** 3012

[15] Bilal M, Gul T, Alsubie A and Ali I 2021 *ZAMM-Journal of Applied Mathematics and Mechanics/Zeitschrift für Angewandte Mathematik und Mechanik* **101** e202000146

[16] Ramesh G K, Madhukesh J K, Prasannakumara B C, Shehzad S A and Abbasi F M 2022 *Arabian J. Sci. Engineer.* **47** 8351

[17] Ullah I, Hayat T, Aziz A and Alsaedi A 2022 *J. Non-Equilibrium Thermodyn.* **47** 61

[18] Ibrahim M, Abidi A, Algehyne E A, Saeed T, Cheraghian G and Sharifpur M 2022 *Sustainable Energy Technologies and Assessments* **49** 101705

[19] Ullah I 2022 *Waves in Random and Complex Media* **1**

[20] Wang F, Xiao Z, Liu X, Ren J, Xing T, Li Z and Chen Y 2022 *Journal of Power Sources* **521** 230925

[21] Gul T, Bilal M, Alghamdi, W, Asjad M I and Abdeljawad T 2021 *Scientif. Rep.* **11**

[22] Gul T, Bilal M, Shuaib M, Mukhtar S and Thounthong P 2020 *Heat Transfer* **49** 3211

[23] Ahmadian A, Bilal M, Khan M A and Asjad M I 2020 *Scientific Reports* **10** 1

[24] Ahmadian A, Bilal M, Khan M A and Asjad M I 2020 *Scientific Reports* **10** 1

[25] Ullah I, Ullah R, Alqarni M S, Xia W F and Muhammad T 2021 *International Communications in Heat and Mass Transfer* **126** 105416

[26] Khashi'ie N S, Arifin N M and Pop I 2022 *Alexandria Engineering Journal* **61** 1938

[27] Alharbi K A M, Ahmed A E S, Ould Sidi M, Ahammad N A, Mohamed A, El-Shorbagy M A and Marzouki R 2022 *Micromachines* **13** 588

[28] Zhao T H, Wang M K and Chu Y M 2021 *J. Math. Inequal.* **15** 701

[29] Bilal M, Saeed A, Gul T, Kumam W, Mukhtar S and Kumam P 2022 *Scientific Reports* **12** 1

[30] Chu Y M, Nazir U, Sohail M, Selim M M and Lee J R 2021 *Fractal and Fractional* **5** 119

[31] Hayat T, Aziz A, Muhammad T and Alsaedi A 2018 *Results in Physics* **9** 290

[32] Li Y X, Shah F, Khan M I, Chinram R, Elmasry Y and Sun T C 2021 *Chaos, Solitons & Fractals* **148** 111010

[33] Ullah I, Hayat T and Alsaedi A 2021 *J. Thermal Analysis Calorimetry* 1–10

[34] Waqas H, Manzoor U, Muhammad T and Hussain S 2021 *Communications in Theoretical Physics* **73** 075006

[35] Chu Y M, Shankaralingappa B M, Gireesha B J, Alzahrani F, Khan M I and Khan S U 2022 *Applied Mathematics and Computation* **419** 126883

[36] Zhao T H, He Z Y and Chu Y M 2020 *AIMS Math.* **5** 6479

[37] Chu Y M, Nazir U, Sohail M, Selim M M and Lee J R 2021 *Fractal and Fractional* **5** 119

[38] Chu Y M, Bashir S, Ramzan M and Malik M Y 2022 *Math. Methods Appl. Sci.*

[39] Ibrahim W, Dessale A and Gamachu D 2021 *Propulsion and Power Research* **10** 180

[40] Kharat P B, Chavan A R, Humbe A V and Jadhav K M 2019 *Journal of Materials Science: Materials in Electronics* **30** 1175

[41] Bilal M, Ayed H, Saeed A, Brahmia A, Gul T and Kumam P 2022 *Waves Random Complex Media* 1–16

[42] Wang X, Ma T B and Ning J G 2014 *Chin. Phys. Lett.* **31** 030201

[43] Haghani F K, Vanani S K and Hafshejani J S 2013 *Chin. Phys. Lett.* **30** 020201

[44] Yildirim A, Gökdoğan A, Merdan M and Lakshminarayanan V 2012 *Chin. Phys. Lett.* **29** 074202

[45] Zhang P and Peng M 2019 *Acta Phys. Sin.* 17

[46] Ma J C, Wei G F and Liu D D 2018 *Chin. Phys. B* **27** 010201

[47] Hong Q, Wang J L and Wang Y S 2018 *Chin. Phys. B* **27** 020202

[48] Cai W J, Wang Y S and Song Y Z 2014 *Chin. Phys. Lett.* **31** 040201

[49] Haghani F K, Vanani S K and Hafshejani J S 2013 *Chin. Phys. Lett.* **30** 020201

[50] Peng-Xuan Z and Miao-Juan P 2019 *Acta Phys. Sin.* **68**

[51] Hong Q, Wang J L and Wang Y S 2018 *Chin. Phys. B* **27** 020202

[52] Ma J C, Wei G F and Liu D D 2018 *Chin. Phys. B* **27** 010201

[53] Hu Y D, Piao J M and Li W Q 2017 *Chin. Phys. B* **26** 094302

[54] Shuaib M, Shah R A and Bilal M 2020 *Advances in Mechanical Engineering* **12** 1687814020936385

[55] Shuaib M, Shah R A, Durrani I, Bilal M 2020 *Journal of Molecular Liquids* **313** 113412

[56] Rashid S, Abouelmagd E I, Sultana S and Chu Y M 2021 *Fractals*

[57] Wang F, Khan M N, Ahmad I, Ahmad H, Abu-Zinadah H and Chu Y M 2022 *Fractals* **30** 2240051

[58] Khan N W, Khan A, Usman M, Gul T, Mouldi A and Brahmia A 2022 *Chin. Phys. B* **31** 064403

[59] Chen S S, Wang J and Li Q H 2016 *Chin. Phys. B* **25** 040203